Soil Dynamics and Earthquake Engineering 140 (2021) 106460

Contents lists available at ScienceDirect

Soil Dynamics and Earthquake Engineering

journal homepage: http://www.elsevier.com/locate/soildyn

Coupled smoothed particle hydrodynamics-discrete element method simulations of soil liquefaction and its mitigation using gravel drains

Usama El Shamy [a,*], Saman Farzi Sizkow [b]

[a] Associate Professor, Civil and Environmental Engineering Dept., Southern Methodist University, PO Box 750340, Dallas, TX, 75275, USA
[b] Graduate Research Assistant, Civil and Environmental Engineering Dept., Southern Methodist University, PO Box 750340, Dallas, TX, 75275, USA

ARTICLE INFO

Keywords:
Smoothed particle hydrodynamics
Discrete element method
Liquefaction
Gravel drains
Liquefaction mitigation
Granular materials

ABSTRACT

In this paper, a fully Lagrangian particle-based method for coupled fluid-particle interaction is utilized to evaluate liquefaction of saturated granular soils subjected to dynamic base excitations. The discrete element method (DEM) is employed to model the solid particles and the fluid motion is simulated using the smoothed particle hydrodynamics (SPH). A coupled SPH-DEM scheme is achieved through local averaging techniques and well-established semi-empirical formulas for fluid-particle interaction. A key feature of the employed technique is that it does not presume undrained conditions for the granular deposit and allows for spatial fluid movements within the deposit. The responses of loose and dense granular deposits to seismic excitation are first analyzed. As expected, the loose deposit exhibited significant pore pressure development and liquefaction while the dense deposit barely showed any considerable buildup of pore pressure and did not liquefy. Liquefaction of the loose deposit resulted in significant surface settlement while that experienced by the dense deposit was within tolerable limits. A liquefaction mitigation technique through the installation of gravel drains was then introduced to the loose deposit and its effect on mitigating pore pressure buildup was examined. Results of conducted simulations show that the installation of gravel drains effectively reduced pore-pressure buildup and, for the most part, the soil maintained its strength. However, the drains did not reduce the overall surface settlement of the deposit to acceptable levels.

1. Introduction

Over the past five decades, the U.S. and other seismically active areas have sustained considerable damage resulting from earthquake-induced site liquefaction that was associated with very costly damage to port facilities, bridges, dams, buried pipes, and buildings of all types. The 2011 Tohoku (Japan) earthquake caused an estimated $300 billion in damage. Evidence of wide spread of liquefaction and lateral spreading at unprecedented scale has been observed in many locations and port facilities [1]. Similarly, the 2010–2011 earthquakes that hit the Christchurch city and its surrounding areas (Canterbury Earthquakes, New Zealand) resulted in a devastating damage due to liquefaction. The most common definition of sand liquefaction is that it is a result of water pressure buildup due to squeezing of pore space during rapid earthquake loading, without sufficient time for water to flow through the grains and drain the pressure [e.g., 2]. That is, when the sand is loosely packed, there would be a tendency for the grains to get into a denser configuration during earthquake motion, squeezing pore-water and rapidly increasing the pressure owing to the high bulk modulus of water.

Liquefaction resistance can be improved by: increasing the soil density through compaction, stabilizing the soil skeleton, reducing the degree of saturation possibly by introducing air bubbles into the void space, dissipation of the generated excess pore pressure, and intercepting the propagation of excess pore pressures buildup, among other techniques. Herein, the focus is on gravel drains as one of the widely used liquefaction hazards mitigation method. Sadrekarimi and Ghalandarzadeh [3] argue that the potential benefits of gravel drains include densification of the surrounding granular soil, dissipation of excess pore water pressure, and redistribution of earthquake-induced or pre-existing stress. They also note that the relatively high internal friction resistance of the gravel imparts a significant frictional component to the treated composite, improving both its strength and its deformational behavior.

Computational modeling offers effective means to predict and assess soil behavior in response to earthquakes. In this regard, the coupled (solid-fluid) response of saturated granular soils is commonly modeled

* Corresponding author.
E-mail addresses: uelshamy@lyle.smu.edu (U. El Shamy), sfarzisizkow@smu.edu (S.F. Sizkow).

https://doi.org/10.1016/j.soildyn.2020.106460
Received 22 August 2020; Received in revised form 7 October 2020; Accepted 9 October 2020
Available online 24 October 2020

using continuum formulations derived based on phenomenological considerations (e.g., the mixture or Biot theories) or homogenization of the micro-mechanical equations of motion [4–6]. Each of these different formulations requires a constitutive model to describe the relationship between effective stresses and strains of the solid phase. For liquefaction problems, constitutive models based on plasticity theory are most commonly used. Several constitutive models have been presented to describe the behavior of saturated granular soils during cyclic loading [e.g, 7–19]. These constitutive relations can be employed in a finite element method or a finite difference formulation to predict the seismic response of a saturated granular deposit. High performance parallel computing simulations have also been presented using continuum-based methods [e.g., 20, 21].

The discrete element method (DEM) provides an alternative effective tool to model granular soils and other geomaterials based on micro-mechanical idealizations. This method [22] simulates these media as assemblages of interacting discrete particles, and has shown great capability to reproduce the actual behavior of granular soils with simple parameters at the microscale. Numerous attempts have been made at incorporating fluid-particle interaction equations into the discrete element method formulation. One of the popular coupling techniques is to describe the fluid flow by averaged Navier-Stokes equation based on mean multiphase mixture properties and employ well-established semi-empirical equations to calculate the fluid particle interaction forces (e.g. Ref. [23,24]). The fluid equations are discretized over a fixed mesh and solved using a technique known as the finite volume method (FVM). This method has proven to yield satisfactory results in simulating different geotechnical phenomena such as soil liquefaction. It has since gained momentum and was adopted by researchers to model several problems in geomechanics [e.g., 25–29]. However, the usage of fixed coarse grid mesh limits its scope and application to the fixed boundary problems.

A more elaborate approach is to model fluid at the pore-scale level to investigate the development of pore pressure due to actual changes in the shape and volume of the pore space caused by particle movements. Zhu et al. [30] developed a pore-scale numerical model using smoothed particle hydrodynamics (SPH) to investigate the flow through porous media. They conducted two-dimensional simulation of flow through periodic arrangements of cylinders and validated the proposed method by comparing the results with those obtained from finite element method. Potapov et al. [31] presented a coupled DEM-SPH method to analyze flows of liquid-solid mixtures. The fluid-particle interaction was obtained by applying no-slip boundary conditions at the solid particles surface. Han and Cundall [32] combined DEM and lattice Boltzmann method (LBM) to simulate flow through porous media at the pore scale. El Shamy and Abdelhamid [33] investigated liquefaction of saturated granular soil deposits by idealizing soil grains through DEM and modeling the pore fluid using LBM. Abdelhamid and El Shamy [34] presented a fully coupled DEM-LBM model to investigate the mechanism of fine particle migration in granular filters. The high accuracy of the pore scale models comes at the price of being computationally expensive, to a degree that makes it impractical to perform numerical simulations with realistic particle sizes using typical desktop computers.

As an alternative to modeling the fluid at the pore scale, SPH could be used to approximate the set of partial differential equations represented by an averaged form of Navier-Stokes equations [35,36] that accounts for the presence of the solid phase and the momentum transfer between the phases. Indeed, SPH is a method that could be generalized to approximate any set of partial differential equations and not necessarily for fluids. For instance, large deformation models of granular materials in a continuum framework have been presented by Chen and Qiu [37], where the saturated soil equations of motions were approximated using SPH. Coupling SPH for the fluid and DEM for the solid phase offers the benefits of overcoming the need for a constitutive model for the solid phase while maintaining the robustness of DEM for large deformation problems and SPH for tracking the fluid motion. Sun et al. [38] presented a Lagrangian-Lagrangian DEM-SPH coupled model for the multiphase flows with free surfaces. They performed dam break and rotational cylindrical tank simulations to showcase the proposed method abilities. Robinson et al. [39] presented a meshless simulation technique based on coupled DEM-SPH algorithm and validated the model by conducting simulations of single particle and constant porosity block sedimentation in a fluid column. Many more examples of coupled DEM-SPH application to various science and engineering problems can be found in the recent literature [40–47].

In this paper, the results of a novel application of SPH-DEM to model soil liquefaction is presented. A key feature of the employed technique is that it does not presume undrained conditions for the granular deposit and allows for spatial fluid movements within the deposit. The responses of loose and dense granular deposits to seismic excitation are first analyzed. As expected, the loose deposit exhibited significant pore pressure development and liquefaction while the dense deposit barely showed any considerable buildup of pore pressure and did not liquefy. A liquefaction mitigation technique through the installation of gravel drains was then introduced to the loose deposit and its effect on mitigating pore pressure buildup was examined.

2. Coupled SPH-DEM Model

A fully coupled Lagrangian particle-based method is presented herein to analyze the dynamic response of saturated granular deposits subjected to horizontal seismic base excitations. In the SPH scheme, the fluid domain is discretized into a set of individual particles carrying local properties of the fluid such as density and pressure [48–50]. DEM is employed to model the solid particles with proper momentum transfer between the two phases. The presented SPH-DEM technique has several advantages over the previously mentioned methods. For instance, the coarse-mesh based nature of FVM-DEM approach requires the use of relatively large cells to ensure presence of enough particles inside them. All particles within each cell are assigned the same porosity which clearly leads to loss of some local features of the porosity field and discrete distribution of porosity throughout the deposit. On the other hand, in SPH-DEM technique, every particle has its unique porosity calculated at its location and it was shown that the right kernel radius can provide a smooth porosity field without losing much of valuable local information [39]. In addition, due to the meshless nature of the SPH-DEM approach, unlike the FVM-DEM technique, it is very well-suited for the deformable boundary problems, irregularly shaped domains, and parallelizing the code is fairly straightforward. The SPH-DEM method also has the advantage of being computationally far less demanding compared to pore-scale models. The main drawback of the presented approach is that the fluid is considered to be weakly compressible. However, the fluctuations in fluid density can be limited to very small values by employing a sufficiently large numerical speed of sound and the fluid can be assumed practically incompressible [51].

A SPH kernel function is utilized to interpolate the averaged forms of continuity and momentum equations over all neighboring particles within the smoothing length of a given point. The fluid pressure is obtained from the weakly compressible equation of state. Therefore, a large value is assigned to the speed of sound to ensure negligible fluctuations in the fluid density. The phase coupling is achieved through semi-empirical relationships between the fluid-particle interaction forces and parameters such as the local porosity and relative velocity between the two phases. These interaction forces are directly applied to the solid particles as external forces and are accounted for in the fluid phase formulation by adding an associated term to the momentum equation. An explicit time integration scheme is used to solve the equation of motion for both solid and fluid particles. Model components are briefly described in the following sections.

2.1. Fluid phase

The two-fluid model presented by Ref. [52] is used here to describe the governing equations for the multiphase mixture [39]:

$$\frac{\partial(n\rho_f)}{\partial t}+\nabla.(n\rho_f\mathbf{u})=0 \tag{1}$$

$$\frac{\partial(n\rho_f\mathbf{u})}{\partial t}+\nabla.(n\rho_f\mathbf{uu})=-\nabla P+\nabla.\boldsymbol{\tau}+n\rho_f\mathbf{g}-\mathbf{f}^{\mathbf{int}} \tag{2}$$

in which ρ_f is the fluid density, n is the porosity, P is the fluid pressure, $\boldsymbol{\tau}$ is the viscous stress tensor, $\mathbf{f}^{\mathbf{int}}$ is the fluid particle interaction force, $\mathbf{g}$ is the gravitational acceleration vector and $\mathbf{u}$ is the fluid velocity.

In SPH, the continuum is lumped into discrete particles moving with the flow and each particle holds the information regarding the physical properties of the fluid. A kernel function (W) is then used to interpolate different quantities at a given location. In this study the Wendland kernel function is chosen as the smoothing function [53].

Applying SPH particle summation, Eqs. 1 and 2 can be rewritten as:

$$\frac{d(n_i\rho_i)}{dt}=\sum_j m_j\mathbf{u_{ij}}.\nabla_i W(|\mathbf{r_{ij}}|,h) \tag{3}$$

$$\frac{d\mathbf{u_i}}{dt}=-\sum_j m_j\left[\frac{P_i}{(n_i\rho_i)^2}+\frac{P_j}{(n_j\rho_j)^2}+R_{ij}\left(\frac{W(|\mathbf{r_{ij}}|,h)}{W(\Delta p,h)}\right)^4\right]\nabla_i W(|\mathbf{r_{ij}}|,h)+\boldsymbol{\Pi}_{ij}+\frac{\mathbf{f}^{\mathbf{int}}}{m_i}+\mathbf{g} \tag{4}$$

with $\mathbf{u_{ij}}$ being the relative velocity vector, P_i fluid pressure evaluated at the location of particle i, r_{ij} the tensile instability term to prevent particles from forming small clumps and $\boldsymbol{\Pi}_{ij}$ the non-artificial viscosity term [54,55].

The weakly compressible equation of state is used to calculate the fluid pressure. This equation provides a relationship between the fluid pressure and its density [51]. In that method, the numerical speed of sound is usually considered to be 10 times higher than the maximum fluid velocity to limit the fluctuations of the fluid density to less than 1% of its initial value.

In this paper, the solid boundaries for SPH particles are treated in the same manner as described by Adami et al. [56]. The implementation of periodic boundaries is rather straight forward in SPH. In this case, the two sides of the model are considered adjacent to each other and, therefore, the truncated support domain of a particle close to one side is completed by contributing particles on the opposite side. In addition, if a particle crosses a periodic boundary it will re-enter the domain from the other side with the same velocity.

2.2. Solid phase

In numerical simulations using discrete element method, it is computationally expensive to use particles with realistic soil grain shapes. Technological advances provide us with more computational power, however, it is still difficult to simulate real granular systems consisting of large numbers of particles without using some forms of simplification. Therefore, particles are usually idealized as spherical bodies to avoid the complications caused by shape irregularity. The importance of rotational inertia on energy dissipation and shear strength of granular materials in quasi-static and dynamic regimes has been proven by both numerical simulations and experimental studies [57–62]. The energy dissipation mechanisms may arise from different micro-mechanical processes in real granular systems, such as adhesion of the contact areas, surface roughness and non-sphericity of particles [63]. To account for the effects of particle shape on the energy loss during rotational particle movements, the rolling resistance contact model was incorporated into DEM simulations by various researchers [59–62].

The rolling resistance contact model employed in this study is based on the linear contact model that incorporates a torque acting on the contacting particles and resisting their rolling motions. The rolling resistance contact model behavior is similar to the linear contact model, except that relative rotation of contacting particles at the contact point produces an internal moment at the contact [59].

2.3. Fluid-solid interaction

The total force exerted by the fluid on the solid particle a can be written as the sum of the drag force ($\mathbf{F_a^D}$) and pressure gradient force ($\mathbf{F_a^P}$) [64]:

$$\mathbf{F_a^{int}}=\mathbf{F_a^D}+\mathbf{F_a^P} \tag{5}$$

The drag force can be estimated through a variety semi-empirical relationships. The well-known equation recommended by Ergun [65] was used in this study. This equation evaluates the drag force based on the local porosity and the relative velocity between fluid and solid particles:

$$\mathbf{F_a^D}=\frac{\beta V_a}{1-n_a}\left(\overline{\mathbf{u}}_\mathbf{a}-\mathbf{u_a}\right) \tag{6}$$

where β is the interphase momentum exchange coefficient, $\overline{\mathbf{u}}_\mathbf{a}$ is the average flow velocity around the solid particle a, V_a is the volume of the solid particle, $\mathbf{u_a}$ is the velocity of the solid particle and n_a is the mean porosity. β follows two different regimes divided by the local porosity ranges [65]:

$$\beta=\begin{cases}150\dfrac{(1-n_a)^2}{n_a}\dfrac{\mu}{d_a^2}+1.75(1-n_a)\dfrac{\rho}{d_a}\left|\overline{\mathbf{u}}_\mathbf{a}-\mathbf{u_a}\right| & n_a\le 0.8\\ 0.75C_d\dfrac{n_a(1-n_a)}{d_a}\rho\left|\overline{\mathbf{u}}_\mathbf{a}-\mathbf{u_a}\right|n_a^{-2.65} & n_a>0.8\end{cases} \tag{7}$$

in which μ is the dynamic viscosity of the fluid, d_a is the solid particle diameter and C_d is the drag coefficient [65].

If the interaction between fluid and solid particles is the only source for the generation of pressure gradient, the total interaction force can be simplified as [64]:

$$\mathbf{F_a^{int}}=\mathbf{F_a^D}+\mathbf{F_a^P}=\frac{\mathbf{F_a^D}}{n_a}-V_a\rho_f\mathbf{g} \tag{8}$$

Due to the momentum exchange with solid particles, a coupling force will also be applied to the fluid particle i which can be estimated by the weighted average of contributions from all surrounding DEM particles inside its influence domain:

$$\mathbf{f_i^{int}}=-\frac{m_i}{\rho_i}\sum_a\frac{W(|\mathbf{r_{ai}}|,h)}{\sum_j\frac{m_j}{\rho_j}W(|\mathbf{r_{aj}}|,h)}\mathbf{F_a^{int}} \tag{9}$$

2.4. Computational scheme

The PFC3D software [63] was used to perform the DEM aspects of the model. The software implements parallel computing for its DEM analysis. The SPH part of the coupled algorithm was carried out by a Cython code written by the authors and linked to the PFC3D environment. Use was made of the Open Multi-Processing (OpenMP) scheme to parallelize the SPH code and reduce the computational time. In addition, to accelerate the neighbor searching process, the fluid domain was divided into cubic cells with sides at least two times larger than the kernel radius (h). All DEM and SPH particles were then mapped into these cells. This way, only a maximum of 27 cells were needed to be probed to find all particles within the support domain of any given SPH particle. Special attention must be paid to the cell size. Using larger cells leads to having more particles inside each cell and slower neighbor searching routines. However, on the other hand, it reduces the number of particle mapping updates required during the simulation. Therefore, an optimum cell size

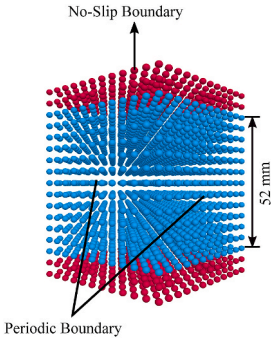

Fig. 1. Initial Poiseuille flow test setup.

creates a balance between the time spent in a single neighbor searching process and the frequency of particle mapping.

The fluid and solid phase equations were solved using explicit time integration schemes. A constant value was selected for the DEM timestep. This value must be smaller than the critical DEM timestep to guarantee stable simulations. The SPH timestep must also satisfy several timestep criteria [54] and is usually larger than the DEM timestep. Therefore, the SPH timestep was assumed to be N times the DEM timestep, where N is an integer. This means that N DEM computation cycles should be performed per one SPH cycle. The first step in a single SPH-DEM computational loop is to calculate the fluid particle properties such as porosity and pressure. The interaction forces are then obtained based on the latest positions and velocities of DEM particles, and the interpolated porosities at their locations. Next, the SPH particle densities, velocities and positions are updated according to the variation rates of density and velocity computed from their pressure, superficial density and the coupling forces. Finally, the interaction forces are applied to the solid particles and N DEM cycles are performed to get the updated particle positions and velocities. The new positions and velocities are then sent as input to the SPH algorithm and the next loop begins.

3. Validation cases

Two validation tests are presented in this section. Poiseuille flow simulation was performed to validate the SPH-based fluid model and examine the performance of the no-slip, no-penetration boundaries. Furthermore, the accuracy of the coupled SPH-DEM model is demonstrated using particle sedimentation test.

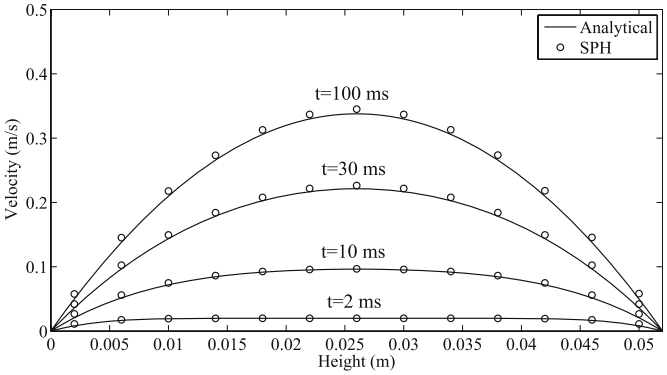

Fig. 3. Comparison between the transient velocity obtained from analytical and numerical solutions for the Poiseuille flow.

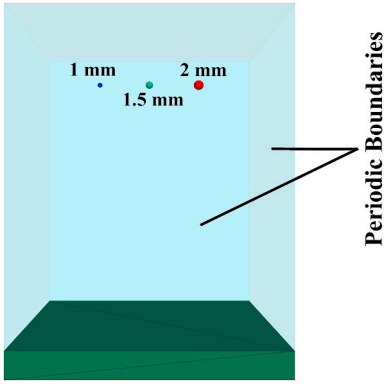

Fig. 4. Initial setup for particle sedimentation test.

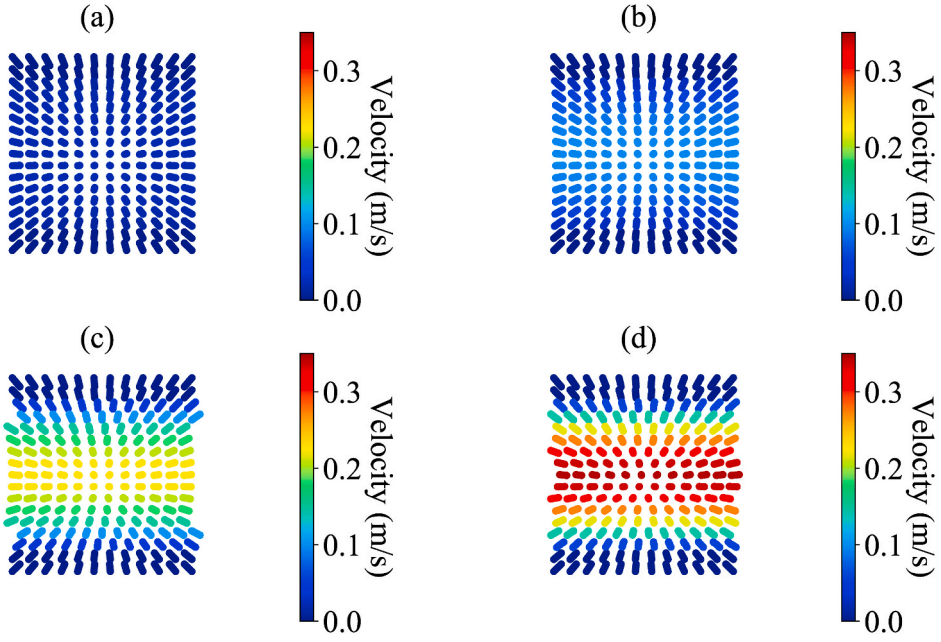

Fig. 2. Side snapshots of the Poiseuille flow model at a) 0.002s, b) 0.01s, c) 0.03s and d) 0.2s.

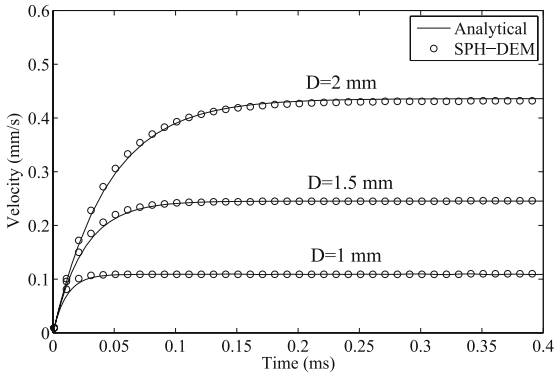

Fig. 5. Comparison between the analytical and numerical results for the vertical velocities of the particles.

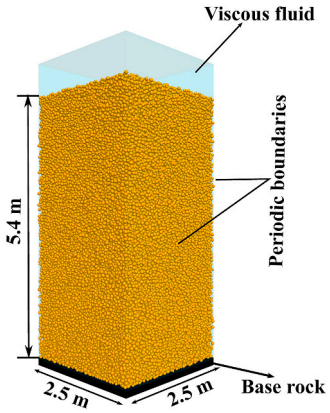

Fig. 6. 3D view of the saturated deposit in conducted simulations.

Table 1
Simulations details in model units.

Soil deposit	
Diameter (sand particles)	1.5 mm–2.5 mm
Diameter (gravel particles)	4.75 mm–6.25 mm
Normal stiffness (sand particles)	5.0×10^5 N/m
Normal stiffness (gravel particles)	1.375×10^6 N/m
Shear stiffness (sand particles)	5.0×10^5 N/m
Shear stiffness (gravel particles)	1.375×10^6 N/m
Normal critical damping ratio	0.1
Shear critical damping ratio	0.0
Friction coefficient	0.5
Rolling friction coefficient	0.2
Density	2650 kg/m^3
Viscous Fluid	
Initial spacing	4 mm
Kernel radius	8 mm
Dynamic viscosity	0.6 Pa s
Density	1000 kg/m^3
Computation parameters	
g-level	30
Time step for DEM	6×10^{-7} s
Time step for SPH	6×10^{-6} s

3.1. Poiseuille flow

This test case model was composed of a fluid column restricted by two parallel plates at the top and bottom. To simulate infinitely extending fluid and plates, the periodic boundary condition was applied to all lateral sides of the model. SPH particles with initial spacing of 4 mm, density of 10^3 kg/m^3 and kinematic viscosity of 10^{-2} m$^2/s$ were used to create the fluid domain with dimensions of $52 \times 48 \times 48$ mm. The solid plates were modeled as no-penetration, no-slip boundaries by two layers of dummy particles with the same spacing as the fluid particles (Fig. 1). To mimic the presence of a pressure gradient of 10 kPa, the initially at rest fluid particles were driven by a body force of 10 m/s^2, which is equal to $\frac{\nabla P}{\rho}$, in the horizontal direction. The analytical solution for the transient fluid velocity can be obtained from the following series [54]:

$$v_y(z,t) = \frac{F_y}{2\nu} z(z-H) + \sum_{n=0}^{\infty} \frac{4F_y H^2}{\nu\pi^3(2n+1)^3} sin\left(\frac{\pi z}{H}(2n+1)\right) exp\left(-\frac{(2n+1)^2\pi^2\nu}{H^2}t\right) \quad (10)$$

in which F_y is the body force, ν is the kinematic viscosity and H is the distance between plates. The side views of the model at four different time instants are presented in Fig. 2. The velocity of the flow is approximately zero in the top and bottom layers which are close to the

Table 2
Soil deposit properties in prototype units.

Saturated unit weight (loose deposit)	19.2 kN/m^3
Saturated unit weight (dense deposit)	19.9 kN/m^3
Porosity (loose deposit)	0.44
Porosity (dense deposit)	0.4
Fundamental frequency (loose deposit)	5.4 Hz
Fundamental frequency (dense deposit)	7.0 Hz
Low strain shear wave velocity (loose deposit)	116 m/s
Low strain shear wave velocity (dense deposit)	151 m/s
Low strain shear modulus (loose deposit)	25.8 MPa
Low strain shear modulus (dense deposit)	45 MPa

Table 3
Amplification factors obtained from DEM solution and analytical expression.

	Loose deposit	
Input Frequency (Hz)	Amplification Factor (DEM)	Amplification Factor (Analytical)
4	2.2	2.5
5	6.43	7.6
6	5.4	4.92
7	2.3	2.12
	Dense deposit	
Input Frequency (Hz)	Amplification Factor (DEM)	Amplification Factor (Analytical)
4	1.57	1.6
5	2.17	2.29
6	3.8	4.3
7	11.9	12.7

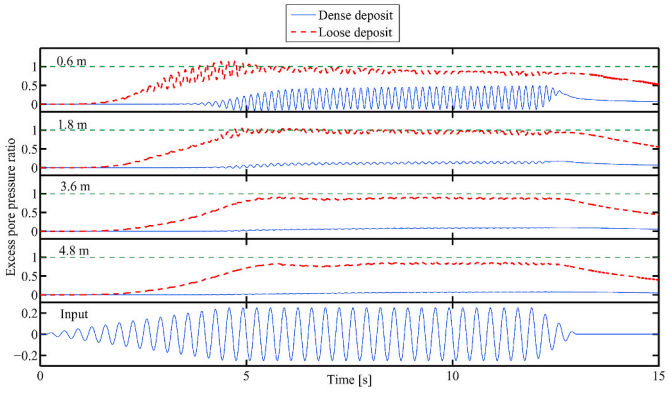

Fig. 7. Time histories of excess pore water pressure at selected depth locations.

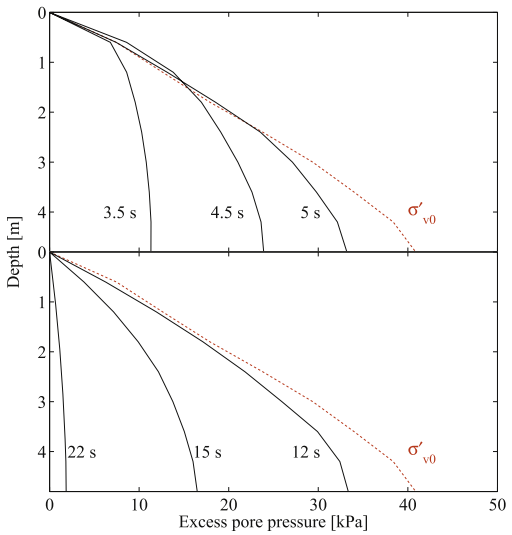

Fig. 8. Excess pore pressure profiles at selected time instants for the loose deposit.

no-slip boundaries and as the time passes the velocity of the fluid increases with its maximum value corresponding to the middle layer. In addition, the particles exiting from the right end return to the domain from the left with the same velocity which verifies the performance of the periodic boundaries. Fig. 3 shows a comparison between the transient velocity obtained from the analytical expression and the numerical simulation. It can be seen that there is a close agreement between the results.

3.2. Particle sedimentation

A particle sedimentation numerical experiment was performed to examine the accuracy of the coupled SPH-DEM algorithm. A fluid column with dimensions of $4.8 \times 4.8 \times 6$ cm was created using SPH particles with initial spacing of 4 mm, density of 10^3 kg/ m^3 and dynamic viscosity of 5.0 Pa s. Three solid particles with density of 2×10^3 kg/ m^3, and radii of 0.5 mm, 0.75 mm and 1 mm were placed within the fluid domain and allowed to settle under the gravitational acceleration of 9.81 m/s^2 (Fig. 4). Assuming $n_a \approx 1$ and $Re \ll 1$, the drag force can be calculated as:

$$F_z^D = 3\pi\mu d_a v_z \tag{11}$$

Using Eq. (11) and solving the differential equation obtained from Newton's second law, the velocity of a falling particle inside a fluid can be computed by:

$$v_z(t) = \frac{2(\rho_p - \rho_f)gr^2}{9\mu}\left[1 - exp\left(-\frac{-9\mu t}{2(\rho_p - \rho_f)r^2}\right)\right] \tag{12}$$

where ρ_p and ρ_f are solid and fluid particle densities, μ is the dynamic viscosity, r is the solid particle radius and g is the vertical gravitational acceleration. Fig. 5 shows a close agreement between the results of the numerical and analytical solutions.

4. Liquefaction of saturated granular soils

The proposed coupled SPH-DEM approach was used to analyze the response of loose and dense saturated granular deposits as well as modeling gravel drains as a measure to mitigate liquefaction of loose sand deposits. In order to realistically model such boundary value problems, some tools have been utilized to bring the simulations to a manageable size. In this regard, use was made of the high g-level concept commonly used in centrifuge testing to decrease the dimensions of the

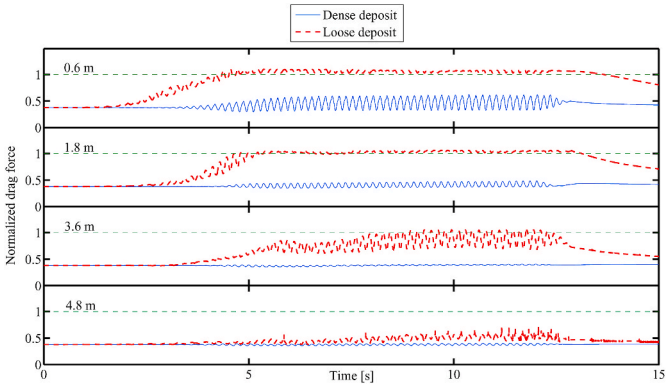

Fig. 10. Time histories of vertical fluid drag force normalized by the average particle weight at selected depths.

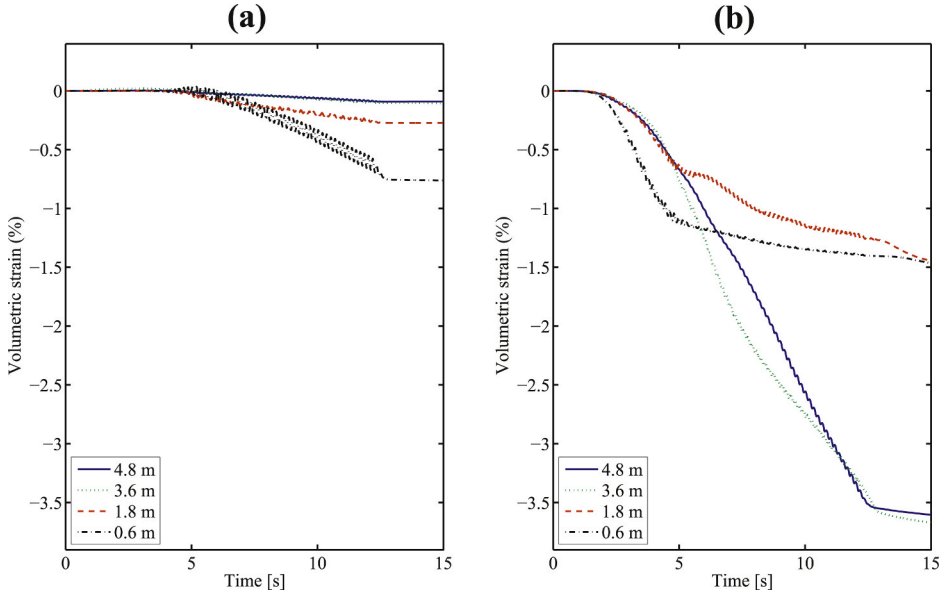

Fig. 9. Time histories of volumetric strains at selected depth locations: (a) dense deposit and (b) loose deposit.

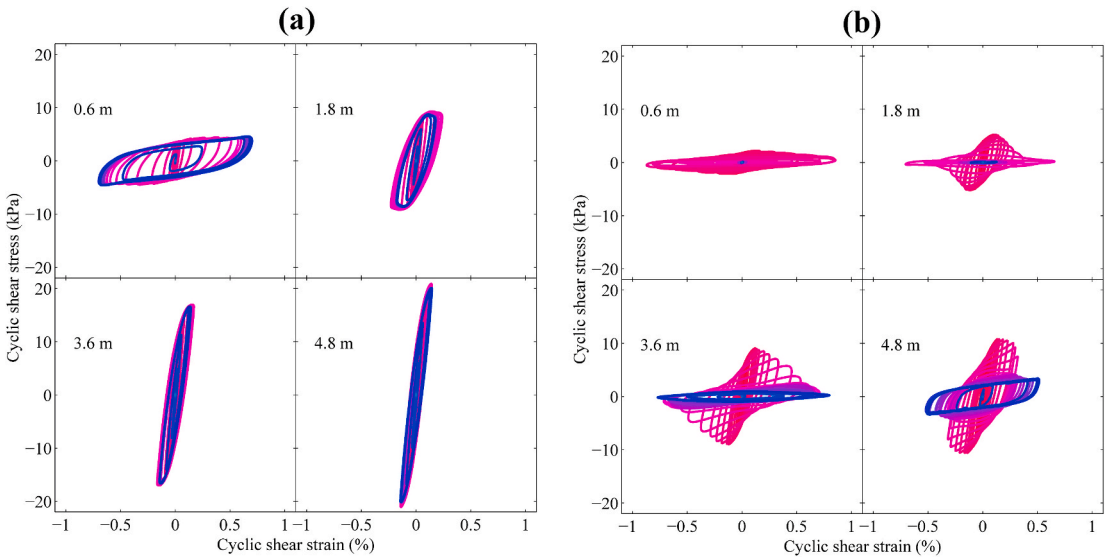

Fig. 11. Shear stress-strain loops at selected depths (the coloring scheme refers to time with dark red being the beginning of shaking and dark blue being the end of the shaking): (a) dense deposit and (b) loose deposit. (For interpretation of the references to color in this figure legend, the reader is referred to the Web version of this article.)

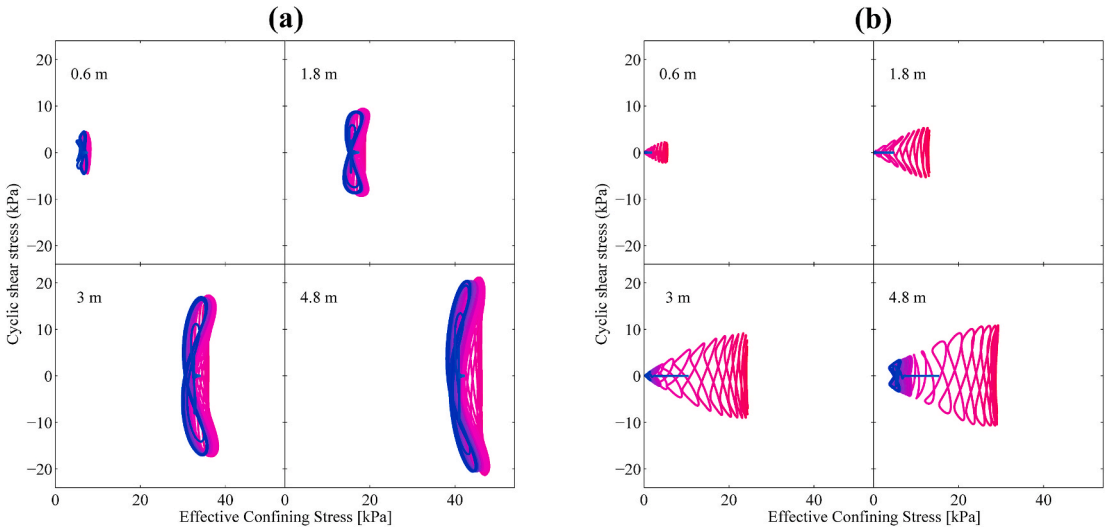

Fig. 12. Time histories of effective stress path at selected depths (the coloring scheme refers to time with dark red being the beginning of shaking and dark blue being the end of the shaking): (a) dense deposit and (b) loose deposit. (For interpretation of the references to color in this figure legend, the reader is referred to the Web version of this article.)

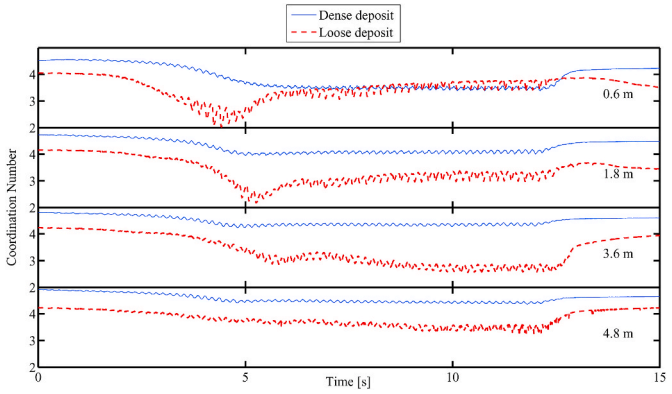

Fig. 13. Time histories of coordination number at the selected depths.

domain that needed to be filled with particles and benefit from a shorter simulation time [66]. This approach was found to be very effective in DEM simulations to model boundary value problems and has been adopted in several applications (e.g. Ref. [23,67]). Additionally, periodic boundaries were employed at the four lateral sides of the model for both DEM and SPH particles to simulate a repeated pattern in an infinite medium with a limited number of particles. The lower boundary, which represents the bedrock, was modeled by a rigid wall in DEM and by a no-slip, impermeable boundary in SPH. One of the advantages of the SPH method is its ability to simulate free surface boundaries without the need of special treatments. Therefore, the free surface condition is automatically applied to the top boundary by filling the domain with fluid particles. The seismic excitations were applied to the fluid and solid phases through the base boundaries.

The simulations were conducted on a 180 mm high (in model units) level deposits. The lateral dimensions of the periodic deposits were chosen to be 84 × 84 mm. The sand particles size range from 1.5 mm to

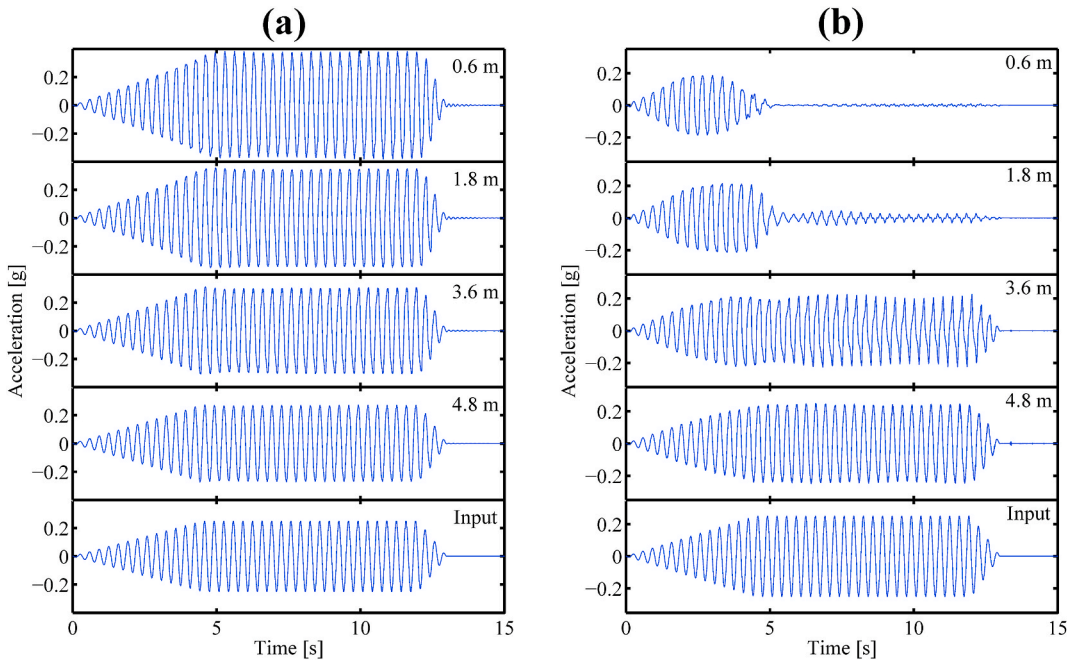

Fig. 14. Time histories of average horizontal acceleration at the selected depths: (a) dense deposit and (b) loose deposit.

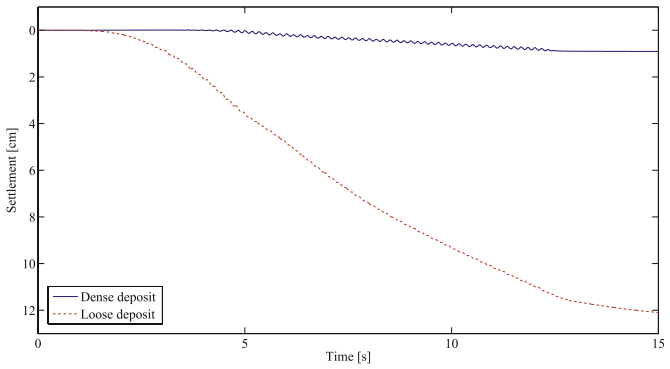

Fig. 15. Time histories of the surface settlement.

2.5 mm, which is close to coarse sand grain size, was used in the creation of the deposits. First, the approximate number of particles needed to fill the domain was calculated. Then these particles were generated in a relatively large space and allowed to settle under the high gravitational field of 30 g. The porosity of the final assembly can be controlled by applying different values to the local damping and/or adjusting the friction coefficient during the particle settlement process. The generated particles were spherical, therefore, rolling friction was employed between them to compensate for their non-realistic shapes. High local damping and friction coefficients were employed during the settlement process to achieve a loose particle packing, then local damping was removed and the friction coefficient was brought down to the target value. The settled loose assembly of particles was found to have an average porosity and saturated unit weight of around 44% and 19.2 kg/ m^3, respectively. The local damping and friction coefficients were removed during the settlement of particles and were added later to reach a dense final state. The dense sand deposit had, respectively, an average porosity and saturated unit weight of around 40% and 19.9 kg/ m^3.

To saturate the deposits, a fluid column with a height of 200 mm (in model units) and same lateral dimensions as the solid deposit was introduced within the periodic domain using SPH particles. The SPH particles with the initial spacing and kernel radius of, respectively, 4 mm and 8 mm, were introduced into the models to create a 6 m (in prototype units) high fluid column and saturate the deposits. The 3D view of the saturated loose deposit is shown in Fig. 6. A high prototype fluid viscosity of 0.02 Pa s was employed to account for the high gravitational field of 30 g and the relatively large particle sizes. For the prototype fluid viscosity of 0.02 Pa s and the employed particle size range, the initial permeability of the deposit was estimated to be 2.9 mm/s (same order of coarse sand permeability when saturated with water) using the Kozeny-Carmen equation [68] for the loose deposit and 1.93 mm/s for the dense deposit.

The deposits were subjected to sinusoidal base excitations with amplitudes of 0.01 g and 0.25 g and a frequency of 3 Hz with a duration of 13 s. The sinusoidal input signal gradually increases until it reaches the maximum acceleration amplitude at 4.5 s, where it remains constant for an additional 7.5 s before it gradually decreases to zero at 13 s. The small amplitude of 0.01 g was selected as an event that was not expected to produce any significant deformations in the system. Simulations conducted with this amplitude are valuable in the determination of the fundamental frequency of the deposit as well as the dynamic soil properties (shear wave velocity and low strain shear modulus). The maximum amplitude of 0.25 g represents a strong seismic event that may induce large deformations and lead to a catastrophic failure. The dynamic properties of the saturated loose and dense deposits were extracted from the results of the simulations with the maximum amplitude of 0.01 g. The shear strains developed within the deposits under this weak excitation were negligible (in the order of 10^{-4}%). A summary of parameters used in the conducted simulations and properties of the soil deposits are provided in Tables 1 and 2. A comparison between the amplification factors at the surface of the loose and dense deposits obtained form DEM simulations (maximum acceleration of 0.01 g) and those of the analytical expression for the transfer of a shear wave propagating in linear elastic soil underlain by rigid bedrock [2] is shown in Table 3. A fair to good agreement between DEM results and the analytical solutions could be concluded form the Table, which further validates the proposed SPH-DEM scheme. Note that the highest amplification factors for the loose deposit were for the shaking frequencies of 5 Hz and 6 Hz, which are close to the fundamental frequency of 5.4 Hz for that deposit. The highest amplification factor for the dense deposit was for the shaking frequency of 7 Hz, which matches its fundamental

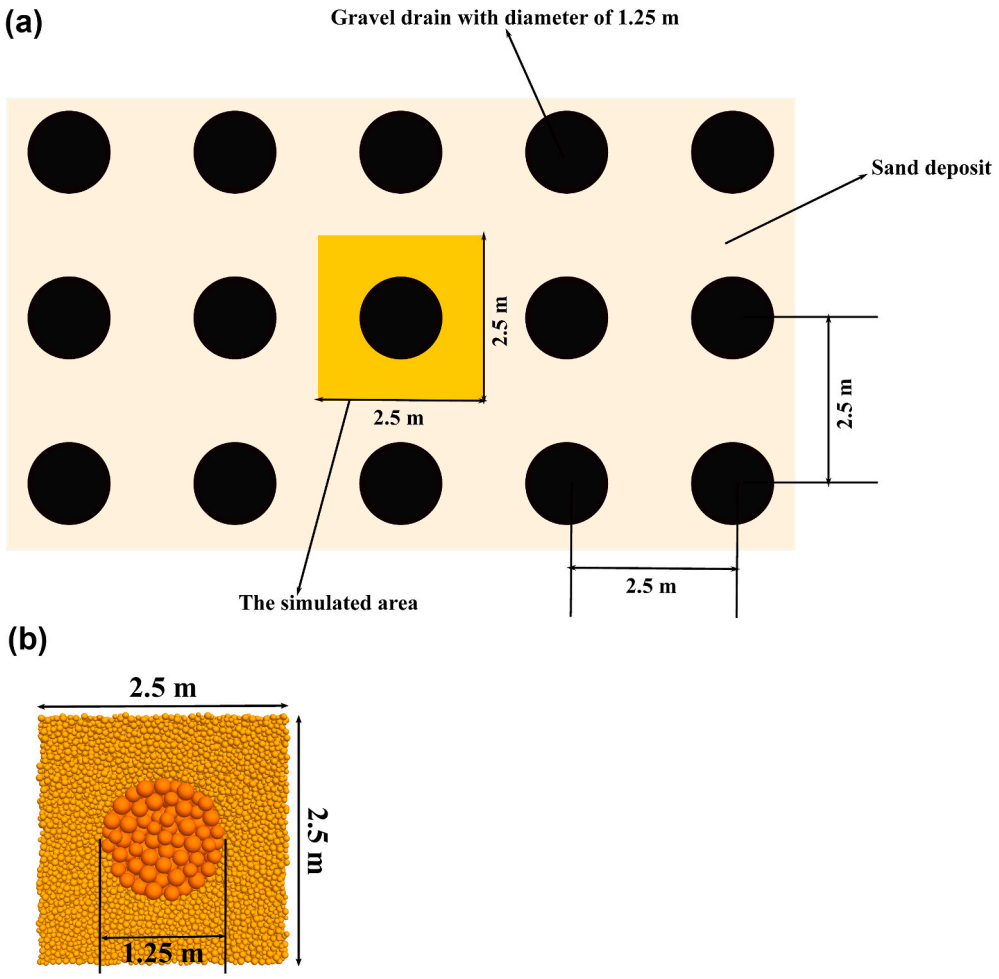

Fig. 16. (a) Schematic plan view of the liquefiable zone and configuration of the gravel drains, and (b) Top view of the deposit and the drain in performed DEM simulation.

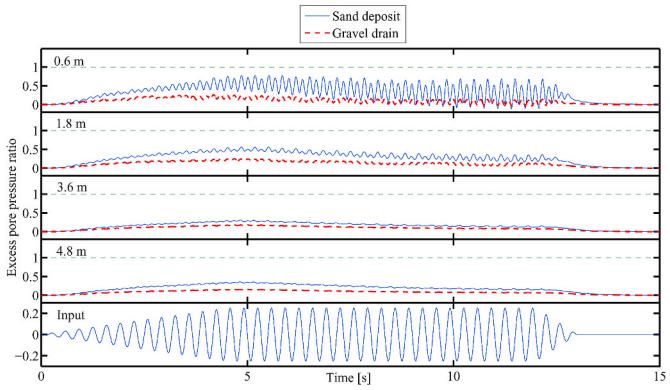

Fig. 17. Time histories of excess pore water pressure at selected depth locations (deposit with the drain).

frequency.

Applying the scaling laws for centrifuge testing results in acceleration frequencies and amplitudes that are 30 times higher in the model while the duration of the loading is 30 times smaller compared to the prototype. Several parameters at various depth locations of the deposit were monitored throughout the simulations such as averaged solid and fluid particle accelerations, averaged excess pore pressure, packing porosity, averaged drag force, stress and strain tensors and coordination number. The data was recorded at constant time intervals of 0.0006 s in model units (0.018 s in prototype units). The simulation results provided in the following sections are in prototype units unless otherwise specified.

4.1. Response of loose and dense deposits

Soil liquefaction is typically marked by a significant buildup of pore pressure and is usually characterized through the pore pressure ratio (the ratio between excess pore water pressure and initial vertical effective stress). A pore-pressure ratio approaching a value of one indicates the excess pressure is counterbalancing the effective stress, leading to complete loss of shear strength. This was not the case for the dense deposit where the pore pressure ratio did not exceed the value of about 0.2 at the 1.8 m depth location and fluctuated between 0 and 0.5 at the 0.6 m depth location because of dilation at that depth (Fig. 7). At deeper depth locations, the pore pressure ratio remained virtually zero. In the case of the loose sand deposit, the top half of the loose sand deposit approached a pore pressure ratio of about 1 and slightly less than 1 for the bottom half, indicating that the entire deposit practically liquified (Fig. 7). This is also confirmed by the excess pore-pressure profiles shown in Fig. 8, which shows the gradual decrease in excess pore pressure as water pressure started to dissipated post shaking.

It is important to highlight the main features of the coupling mechanism between the fluid and solid particles in the presented SPH-DEM technique. Herein, pore pressure develops due to volumetric strains (changes in porosity with respect to initial value). The volumetric strains

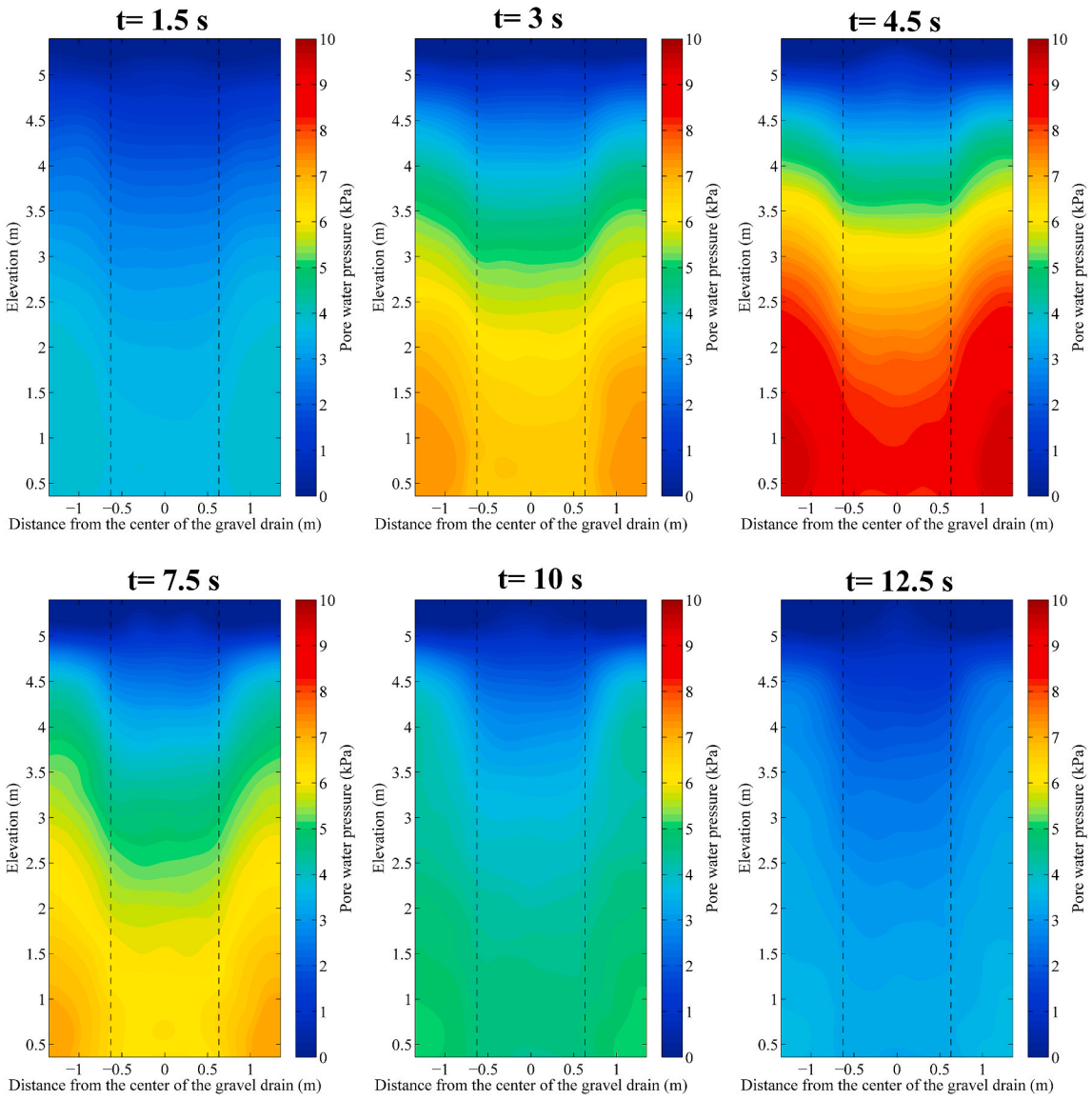

Fig. 18. Excess pore pressure contours at selected time instants (deposit with the drain).

were monitored in performed simulations and are plotted in Fig. 9. In the case of dense sand, the magnitude of volumetric strains in the deeper depth locations was very small (less than 0.2%) and reached about 0.75% near the surface (Fig. 9a). This explains why there was no significant pore pressure buildup in the case of dense sand. The magnitude of volumetric strains in the case of loose sand reached values as high as 3.5%. The reduction in the volume of pore space and subsequent pore pressure buildup is in agreement with a more fundamental pore-scale modeling using LBM-DEM simulations [33,69].

Another important feature of the SPH-DEM framework is that the developed pore pressures form pressure gradients as shown in Fig. 8 that results in upward drag forces that counterbalance the weight of the particles. Fig. 10 shows these drag forces normalized by the weight of the particles at different depth locations along the dense and looses deposits. A normalized drag force value of one indicates that the fluid is essentially carrying the particles and the effective stresses would approach zero. In the dense deposit, the normalized drag force was about the value corresponding to the submerged state of the particles and did not practically increase beyond that level except very near the surface. In the loose deposit, the magnitude of the normalized drag force approached the value of one at all depth locations except near the base, indicating liquefaction has occurred at those upper depth locations.

Liquefaction is a state of instability that is marked by vanishing effective confining pressure and shear stresses as well as the development of large strains. Fig. 11 shows the shear stress-strains histories for the dense and loose sand deposits. Except for the 0.6 m depth location, there was no significant reduction in shear stresses and induced shear strains for the dense deposit (Fig. 11a). Therefore, shear stiffness degradation was minimal for the case of dense sand. A contrasting behavior can be seen for the loose deposit where significant reduction in shear stresses and stiffness was observed as well as shear strains approaching values as large as 0.7% (Fig. 11b). Plots of the effective confining stress paths at different depth locations for the two deposits are shown in Fig. 12, where there was marginal reduction in effective confining pressure in the case of dense sand (Fig. 12a). On the other hand, significant reduction in mean confining pressure (completely vanishing in top levels) was observed in the case of loose sand (Fig. 12b).

A different way of looking at the instability encountered during liquefaction is to check the particles packing in terms of average number of contacts per particle at a specific location in the assembly, which is known as the coordination number. The higher the coordination number, the more stable the assembly is and vice versa. A minimum value of 4 is needed for a stable frictional assembly under static conditions [70]. This criterion could be used (as a first approximation) to assess the

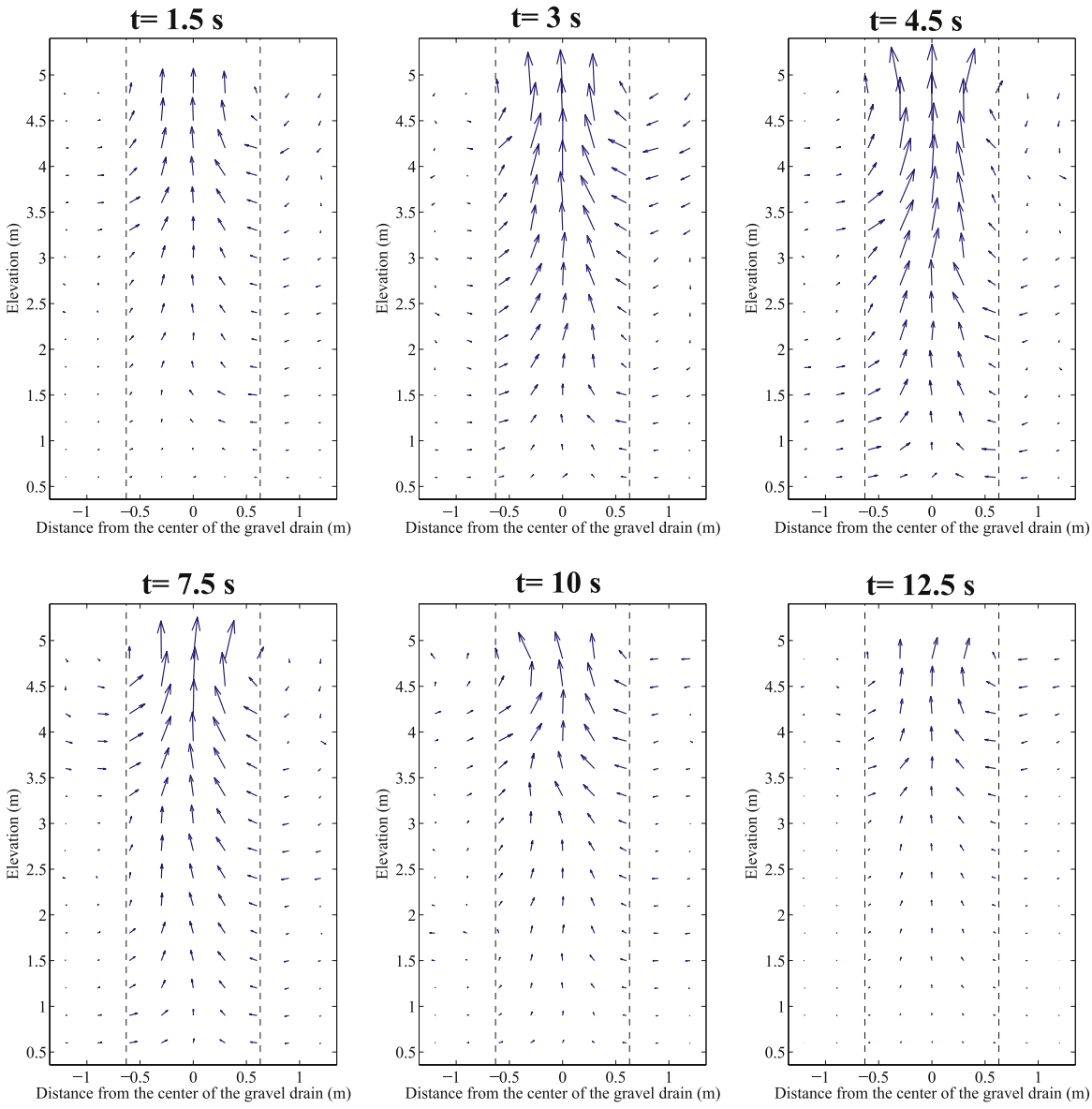

Fig. 19. Relative fluid velocity field at selected time instants (deposit with the drain).

stability of the packing as the deposit underwent base shaking. Fig. 13 shows time histories of the evolution of the coordination number at selected depth locations along the dense and loose deposits. The initial value of the coordination number was higher for the dense deposit compared to the loose deposit. As shaking progressed, significant drop in coordination number was observed in the loose deposit compared to the dense deposit, which maintained a coordination number higher than 4 except at the 0.6 m depth location. At that depth, the vertical overburden pressure is very small and the sand could become instantaneously unstable during shaking. In practice, the groundwater table will be below the ground level and the overburden pressure would be higher and it would be unlikely for the dense sand to become unstable.

The computed horizontal acceleration time histories are shown in Fig. 14. The acceleration time histories for the case of the dense sand showed amplification as the motion traveled to the surface (Fig. 14a). The acceleration vanished for the top half of the loose deposit and maintained an amplitude close to the input base motion for the bottom half (Fig. 14b). This is because particles in the bottom half did not fully lose contact and were still able to transmit the base motion (see Fig. 13). Fig. 15 shows the settlement experienced by the dense and loose deposits by the end of shaking. The total settlement of the dense deposit was less than 1 cm, which is considered acceptable from an engineering design point of view. The total settlement of the loose deposit was about 12.5 cm, which is obviously not acceptable for design purposes.

4.2. *Effect of gravel drains*

In order to model the gravel drains, the arrangement shown in Fig. 16a, which shows a schematic plan view of the simulated area, was considered as a liquefaction mitigation plan. The gravel drains with radii of 1.25 m are placed throughout the sand deposit at 2.5 m intervals center-to-center. Due to the symmetrical configuration of the drains, a small periodic domain enclosing one of the gravel drains was modeled in this study (Fig. 16b). The selected periodic domain had a height of 5.4 m with lateral dimensions of 2.5 m by 2.5 m (all in prototype units). To install the gravel drain, first the sand particles inside a cylinder with a diameter of 1.25 m aligned with the vertical central axis of the deposit were removed and a hollow cylindrical rigid wall with the same diameter was placed inside the hole to support the surrounding soil. The gravel particles with the size range of 4.75 mm–6.25 mm were generated inside the cylindrical wall and settled under the strong gravitational field. Then, the cylindrical wall was removed and the assembly of

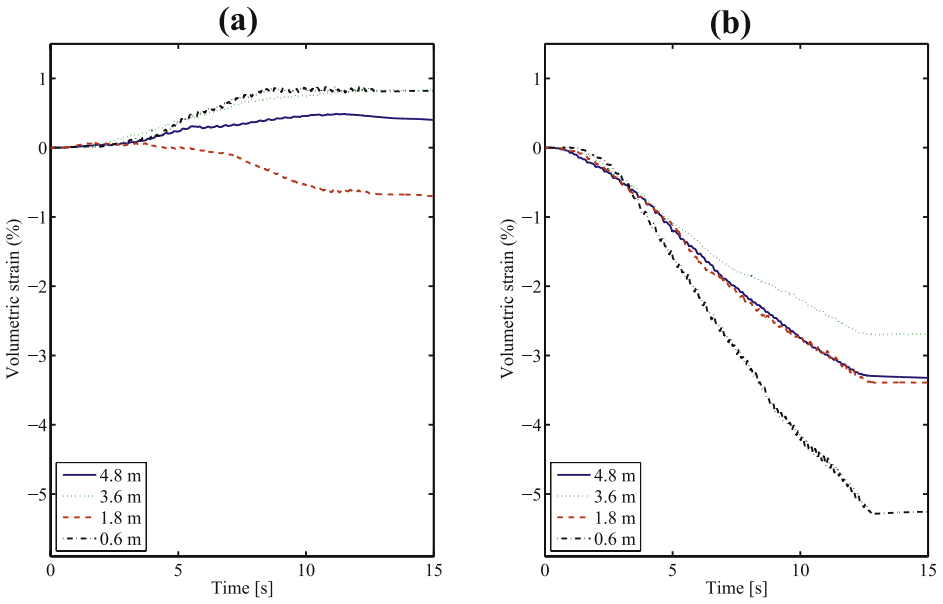

Fig. 20. Time histories of volumetric at selected depth locations: (a) inside the gravel drain, and (b) within the surrounding sand.

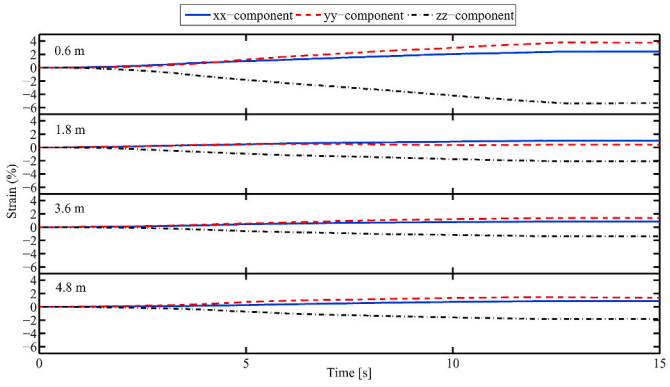

Fig. 21. Time histories of normal strains at selected depth locations inside the gravel drain.

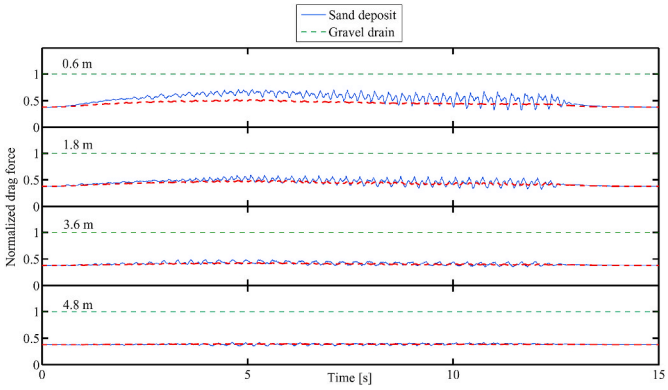

Fig. 23. Time histories of vertical fluid drag force normalized by the average particle weight at selected depths (deposit with the drain).

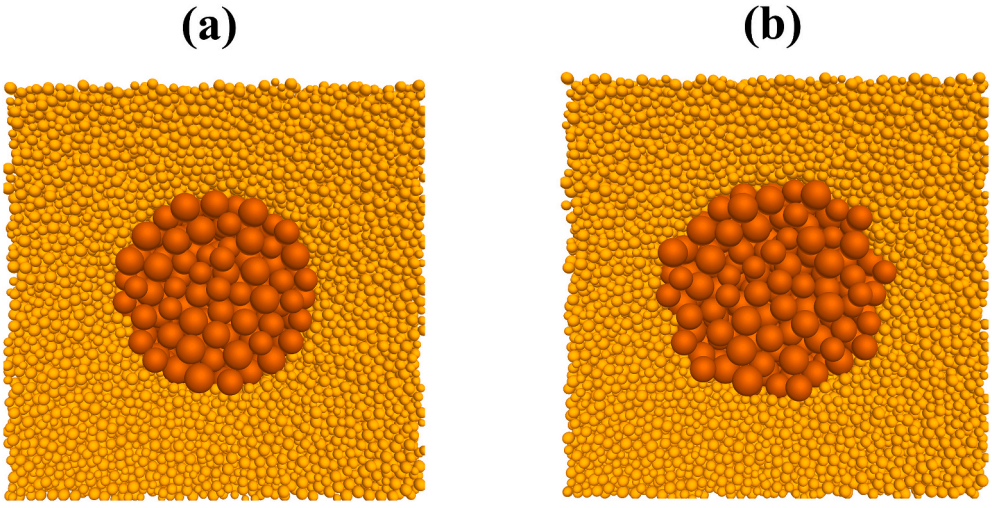

Fig. 22. Top views of the gravel drain deposit: (a) before shaking, and (b) after shaking.

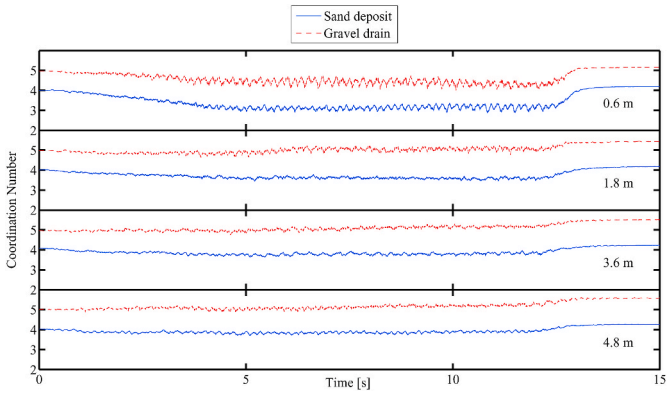

Fig. 24. Time histories of coordination number at selected depths (deposit with the drain).

particles was allowed to reach equilibrium. Even with the larger particle size of the gravel compared to the sand, the permeability of the drain was not enough to mitigate the excess pore pressure. Therefore, the gravel permeability was increased through a reduction in the fluid drag force (in other words, reducing the resistance to flow). According to Ergun [65], the pressure gradient can be shown as:

$$\nabla P = 150\frac{(1-n)^2}{n^2}\frac{\mu}{d_p^2}\mathbf{u} + 1.75\frac{1-n}{n}\frac{\rho}{d_p}\mathbf{u}|\mathbf{u}| \tag{13}$$

in which **u** is the relative fluid velocity. Using Eq. (7) for $n \leq 0.8$ we obtain:

$$\mathbf{u} = \frac{n}{\beta}\nabla P \tag{14}$$

It is obvious from Eq. (14) that the permeability of soil is inversely related to β. Therefore, in order to further increase the permeability of the drain, the interphase momentum exchange coefficient (β) is reduced by a factor of 10 inside the drain to artificially increase the permeability. The resulting permeability of the gravel drain was about 105 mm/s in prototype units, which is almost 36 times higher than the permeability of the loose sand deposit. According to the design criteria provided by Onoue [71], the arrangement shown in Fig. 16a and the properties of the system should effectively reduce the excess pore pressure ratio of the sand to values below 0.5.

Time histories of excess pore-pressure ratio along the depth of the drain as well as the neighboring sand are shown in Fig. 17. Compared to Fig. 7, there has been considerable reduction in developed pore pressure but it was not completely eliminated by the presence of the drain. The pressure outside the drain was relatively higher than inside, indicating the fluid is migrating into the drain. It was of interest to investigate the patterns of fluid pressure and associated migration in the deposit. The fluid pressure contours and velocity field are plotted, respectively, in Figs. 18 and 19 along a section passing through the center of the drain and perpendicular to the direction of shaking. The perpendicular direction was selected because the phase lag between the computed quantities on a plane in the direction parallel to shaking made it difficult to provide meaningful plots. The snapshots of the fluid pressure distribution clearly show that the pressure outside the drain is higher, suggesting that the fluid motion could be responding to that pressure difference (Fig. 18). The snapshots show how the pressure buildup continued as the base shaking progressed and reached its maximum at about 4.5 s, then started to dissipate from that instant. A sharp reduction to almost no excess pore pressure could be noticed at the 12.5 s mark as the shaking reduced in amplitude. Fig. 19 depicts the relative, with respect to solid particle, fluid velocity vectors (the horizontal velocities were scaled up to make them more visible) and clearly indicates that the fluid migrated from the parts of the sand close to the drain into the gravel drain. The Figure also shows how the amplitude of the relative fluid velocities increased as shaking progressed. Fluid velocities inside the drain could be seen clearly migrating vertically towards the surface. Note that the large amplitude of the vertical velocity inside the drain compared to the small amplitude of horizontal velocities is because fluid is coming into the drain across the surface area of the cylindrical drain (which is more than 17 times higher than the cross sectional area of the drain itself).

The volumetric strains developed inside the gravel drain and the surrounding sand are shown in Fig. 20. The gravel experienced mostly volume increase, except for the 1.8 depth location that underwent

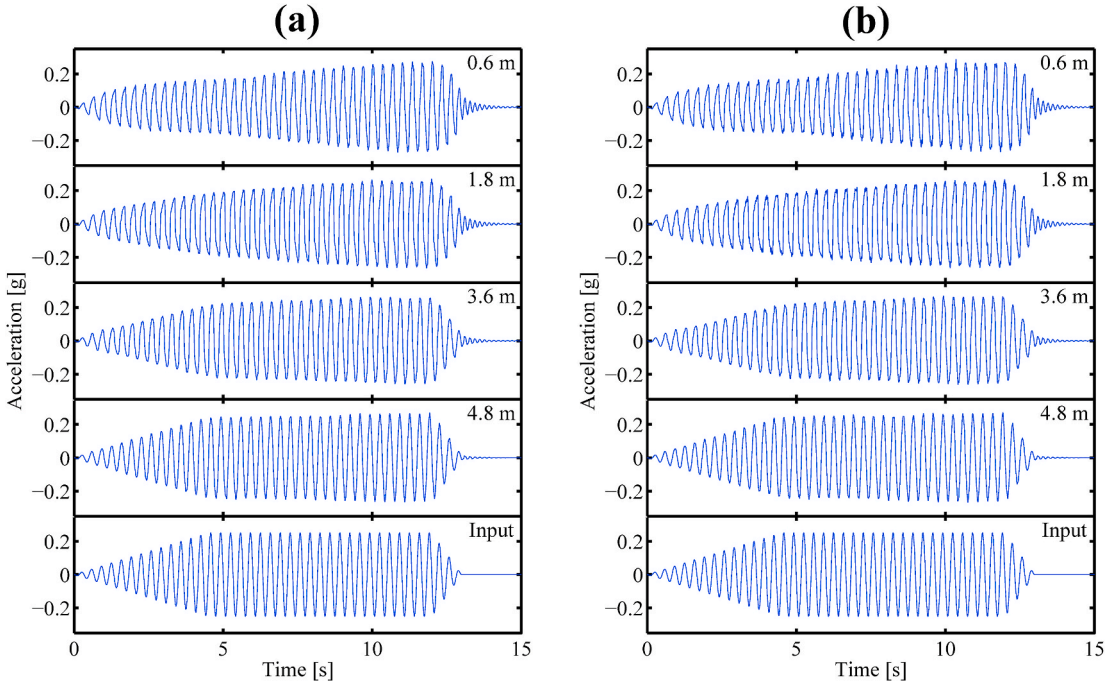

Fig. 25. Time histories of average horizontal acceleration at selected depths: (a) inside the gravel drain, and (b) within the surrounding sand.

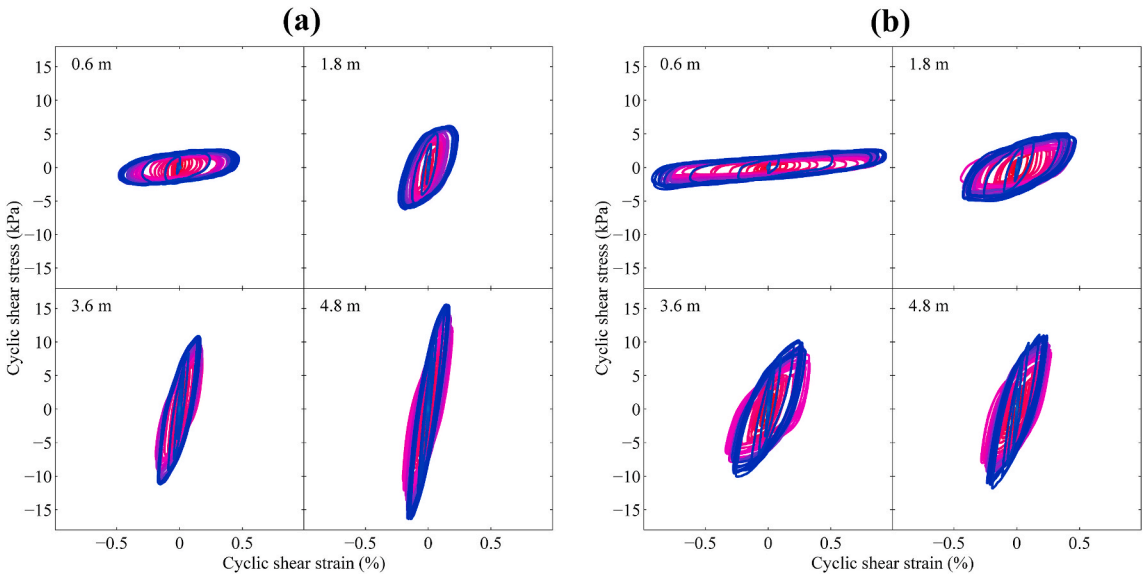

Fig. 26. Shear stress-strain loops at selected depths: (a) inside the gravel drain, and (b) within the surrounding sand.

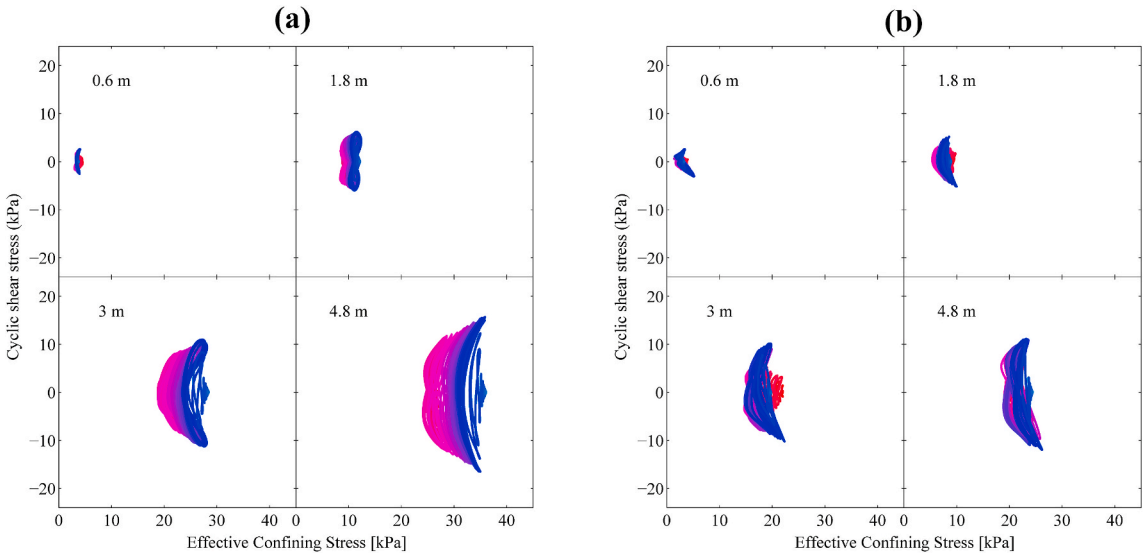

Fig. 27. Time histories of effective stress path at selected depths: (a) inside the gravel drain, and (b) within the surrounding sand.

contraction (Fig. 20a). The sand on the other hand, showed significant contraction at all depth locations (Fig. 20b). Further investigation of the volume expansion of the gravel revealed that the expansion is taking place in the lateral directions (Fig. 21). That is, the drain expanded radially as shaking progressed and the gravel pushed the loose sand aside. This is also confirmed from Fig. 22 where it shows a top view of the drain before shaking and its expansion post shaking.

The vertical drag forces exerted by the fluid on the gravel and sand particles remained mostly within the submerged fraction of the weight of the solid particles (Fig. 23), indicating liquefaction did not occur in the sand nor the gravel. This is confirmed by the relatively high values of coordination number that remained above the value of 4 at most of the depth locations of the sand (expect very near the surface) and all the depth locations along the gravel drain (Fig. 24).

The relatively stable packing of particles demonstrated by the high coordination numbers resulted in full transmission of the ground motion from the base rock to the surface (Fig. 25). The acceleration amplitude at the corresponding depth locations between the gravel and sand were comparable as the gravel drains results in a stiffening effect for the whole deposit. That is, the motion of the non-liquefied gravel dictated the lateral acceleration of the whole deposit. However, there was no sign of motion amplification as was the case of the dense sand deposit.

The shear stress-strain loops indicated stiffness reduction and large shear strains at locations near the surface in both the gravel and sand portions of the deposit (Fig. 26) without loss of strength. At deeper depth locations, the level of strains experienced by the sand were smaller than the case with no gravel drain treatment. The effective stress paths at different locations along the deposit confirm that there was no loss of strength marked by values of effective confining pressure approaching zero (Fig. 27). The effective stress path at the depth locations from 1.8 m to 4.8 m exhibited an unfamiliar pattern. There was an increase in confining pressure as shaking progressed. In addition, the initial magnitude of the confining pressure in the sand deposit (Fig. 27b) at deep depth location was significantly smaller than the corresponding locations in the untreated loose sand (Fig. 12b). This trend continued as shaking progressed. The reduction in the stresses in the sand surrounding the gravel drain are attributed to the downdrag (also known as negative skin friction) imposed by the loose sand on the dense gravel

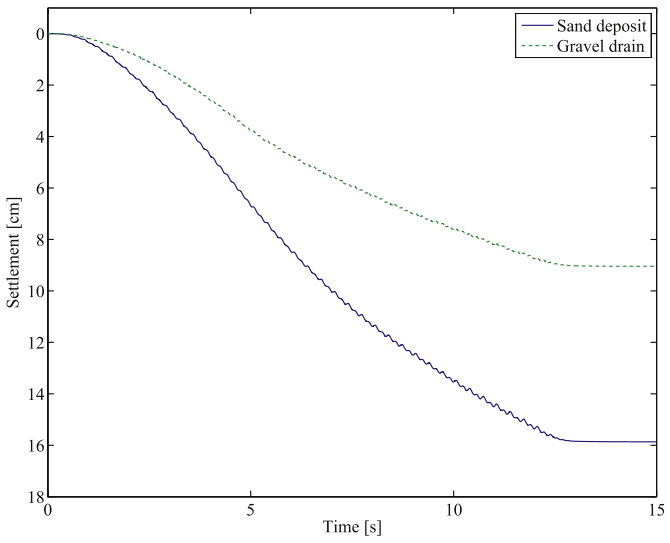

Fig. 28. Time histories of the surface settlement (deposit with the drain).

columns. As the gravel drain was made of dense packing and hence less susceptible to further settlement, the sand particles transmitted some of their weight to the gravel drain by friction as they underwent further settlement after the construction of the drain and during shaking of the deposit.

The total surface settlement of the deposit at points near the surface of the drain and the neighboring sand are shown in Fig. 28. The surface settlement at the top of the gravel drain was about 9 cm compared to about 16 cm at the surface of the sand. One could conclude that the overall settlement of the site has slightly improved compared to the untreated loose sand deposit (settlement reduced from 12.5 cm to 9 cm), since practically the foundation soil would be considered that of the gravel drains. However, this improved settlement magnitude still exceeds the acceptable limits by most code provisions. This observation agrees with the work of Brennan and Madabhushi [72] who noted that settlement can still occur to an unsatisfactory degree when the drains were used to remediate the soil under shallow foundations. It should also be noted that the settlement of the sand surrounding the drain was higher than the untreated site. This is because of the void space that was created between the sand and the perimeter of the gravel drain during the numerical installation of the drain. In practice, the gravel would likely be compacted to ensure high density gravel and further densify the surrounding sand. In the performed simulations, it was opted not to compact the gravel so that the surrounding sand remain loose as well as susceptible to liquefaction, and the effectiveness of the gravel drain could be assessed.

5. Conclusions

A three-dimensional fully coupled particle-based model is presented to evaluate the dynamic response and liquefaction of saturated granular deposits and the use of gravel drains as a liquefaction mitigation measure. A microscale idealization of the solid phase is achieved using the discrete element method while the fluid phase is modeled using the smoothed particle hydrodynamics. In this method, the interstitial pore fluid is idealized using averaged Navier-Stokes equations and the fluid-particle interaction forces are quantified using well-known semi-empirical relationships. The presented model is computationally far less demanding compared to the pore-scale level models and its meshless nature makes it a powerful tool for analyzing moving boundary, irregularly shaped domains, and free surface problems. A key feature of the employed technique is that it does not presume undrained conditions for the granular deposit and allows for spatial fluid movements within the deposit. The proposed approach was used to model the responses of loose and dense granular deposits to seismic excitation as well as modeling gravel drains as a measure to mitigate liquefaction hazards. The loose deposit experienced liquefaction marked by several response mechanisms including excess pore-pressure buildup approaching the value of one, increase in the vertical drag forces that counterbalance the weight of solid particles, reduction of averaged coordination number causing the instability of the packing, diminishing averaged particle acceleration time histories, continuous degradation of soil stiffness and strength, as well as large surface settlement. The dense deposit, on the other hand, barely showed any considerable buildup of pore pressure, did not liquefy and developed relatively small surface settlement. The installation of gravel drains effectively reduced pore-pressure buildup and for the most part the soil maintained its strength. The gravel drains experienced radial expansion during shaking as gravel grains pushed the loose sand particles aside. Pore pressure distribution showed less pore pressure developed in the drain compared to neighboring sand and fluid migrating from the sand to the gravel drain. Fluid velocities inside the drain were mostly migrating vertically towards the surface. However, the presence of the drain did not reduce surface settlement to acceptable service limits. It should be noted that these observations pertain only to the conditions considered herein and more research is needed to model the effect of particle size (for the gravel and sand deposit) as well as the effect of compacting the gravel columns on the response of the system.

CRediT authorship contribution statement

Usama El Shamy: Conceptualization, Methodology, Investigation, Supervision, Writing - original draft. **Saman Farzi Sizkow:** Data curation, Visualization, Writing - review & editing.

Declaration of competing interest

The authors declare that they have no known competing financial interests or personal relationships that could have appeared to influence the work reported in this paper.

Acknowledgement

This research was partially supported by the US Army Corps of Engineers Engineer Research and Development Center, grant number W9132V-13-C-0004 and the National Science Foundation award number CMMI-1728612. These supports are gratefully acknowledged.

References

[1] Meneses J, Arduino P. Preliminary observations of the effects of ground failure and tsunami on the major ports of Ibaraki prefecture. Technical Report GEER-025c, Geotechnical Extreme Events Reconnaissance. (GEER) Association; 2011.
[2] Kramer S. Geotechnical Earthquake Engineering. Englewood Cliffs, NJ: Prentice-Hall; 1996.
[3] Sadrekarimi A, Ghalandarzadeh A. Evaluation of gravel drains and compacted sand piles in mitigating liquefaction. Ground Improv 2005;9(3):91–104.
[4] Lewis RW, Schrefler BA. The Finite Element Method in the Deformation and Consolidation of Porous Media. New York, USA: Wiley; 1987.
[5] Zienkiewicz OC, Chan AHC, Pastor M, Schrefler BA, Shiomi T. Computational Geomechanics with Special Reference to Earthquake Engineering. England: John Wiley and Sons; 1998.
[6] Arduino P, Macari EJ. Implementation of porous media formulation for geomaterials. J Eng Mech 2001;127(2):157–66.
[7] Elgamal A, Parra E, Ragheb A, Yang Z. Modeling of cyclic mobility in saturated cohesionless soils. Int J Plast 2003;19(6):883–905.
[8] Elgamal AW, Yang Z, Parra E. Computational modeling of cyclic mobility and post-liquefaction site response. Soil Dynam Earthq Eng 2002;22:259–71.
[9] Prevost J. A simple plasticity theory for frictional cohesionless soils. Soil Dynam Earthq Eng 1985;4(1):9–17.
[10] Taiebet M, Dafalias YF, Peek R. A destructuration theory and its application to SANICLAY model. Int J Numer Anal Methods GeoMech 2010;34(10):1009–40.
[11] Dafalias YF, Manzari MT. Simple plasticity sand model accounting for fabric change effects. J Eng Mech 2004;130(6):622–34.
[12] Andrade JE, Borja RI. Modeling deformation banding in dense and loose fluid-saturated sands. Finite Elem Anal Des 2007;43(5):361–83.

[13] Byrne PM, Seid-Karbasi M. Seismic liquefaction, lateral spreading, and flow slides: a numerical investigation into void redistribution. Can Geotech J 2007;44(7):873–90.
[14] Boulanger RW, Ziotopoulou K. Formulation of a sand plasticity plane-strain model for earthquake engineering applications. Soil Dynam Earthq Eng 2013;53:254–67.
[15] Ziotopoulou K, Boulanger RW. Calibration and implementation of a sand plasticity plane-strain model for earthquake engineering applications. Soil Dynam Earthq Eng 2013;53:268–80.
[16] Wang Rui, Zhang Jian-Min, Wang Gang. A unified plasticity model for large post-liquefaction shear deformation of sand. Comput Geotech 2014;59:54–66.
[17] Zou You-Xue, Zhang Jian-Min, Wang Rui. Seismic analysis of stone column improved liquefiable ground using a plasticity model for coarse-grained soil. Comput Geotech 2020;125:103690.
[18] Tasiopoulou P, Gerolymos N. Constitutive modelling of sand: a progressive calibration procedure accounting for intrinsic and stress-induced anisotropy. Geotechnique 2016;66(9):754–70.
[19] Barrero Andres R, Taiebat Mahdi, Dafalias Yannis F. Modeling cyclic shearing of sands in the semifluidized state. Int J Numer Anal Methods GeoMech 2020;44(3):371–88.
[20] Lu J, Elgamal A, Yan L, Law KH, Conte JP. Large scale numerical modeling in geotechnical earthquake engineering. Int J GeoMech 2009. https://doi.org/10.1061/(asce)gm.1943-5622.0000042.
[21] Peng J, Lu J, Elgamal A, Law KH. ParCYCLIC: finite element modeling of earthquake liquefaction response on parallel computers. Int J Numer Anal Methods GeoMech 2004;28(12):1207–32.
[22] Cundall P, Strack ODL. A discrete numerical model for granular assemblies. Geotechnique 1979;29(1):47–65.
[23] El Shamy U, Zeghal M. Coupled continuum-discrete model for saturated granular soils. J Eng Mech 2005;131(4):413–26.
[24] El Shamy U, Zeghal M, Dobry R, Thevanayagam S, Elgamal A, Abdoun T, Medina C, Bethapudi R, Bennett V. Micromechanical aspects of liquefaction-induced lateral spreading. Int J GeoMech 2010;10(5):190–201.
[25] Chen F, Drumm EC, Guiochon G. Coupled discrete element and finite volume solution of two classical soil mechanics problems. Comput Geotech 2011;38(5):638–47.
[26] Liu G, Rong G, Peng J, Zhou C. Numerical simulation on undrained triaxial behavior of saturated soil by a fluid coupled-DEM model. Eng Geol 2015;193:256–66.
[27] Guo Y, Yu XB. Understanding the microscopic moisture migration in pore space using DEM simulation. J. Rock Mech. Geotechn. Eng. 2015;7(2):171–7.
[28] Ravichandran N, Machmer B, Krishnapillai H, Meguro K. Micro-scale modeling of saturated sandy soil behavior subjected to cyclic loading. Soil Dynam Earthq Eng 2010;30(11):1212–25.
[29] Okada Y, Ochiai H. Coupling pore-water pressure with distinct element method and steady state strengths in numerical triaxial compression tests under undrained conditions. Landslides 2007;4(4):357–69.
[30] Zhu YI, Fox PJ, Morris JP. A pore-scale numerical model for flow through porous media. Int J Numer Anal Methods GeoMech 1999;23(9):881–904.
[31] Potapov AV, Hunt ML, Campbell CS. Liquid–solid flows using smoothed particle hydrodynamics and the discrete element method. Powder Technol 2001;116(2–3):204–13.
[32] Han Y, Cundall PA. Lattice Boltzmann modeling of pore-scale fluid flow through idealized porous media. Int J Numer Methods Fluid 2011;67(11):1720–34.
[33] El Shamy U, Abdelhamid Y. Modeling granular soils liquefaction using coupled lattice Boltzmann method and discrete element method. Soil Dynam Earthq Eng 2014;67:119–32.
[34] Abdelhamid Y, El Shamy U. Pore-scale modeling of fine-particle migration in granular filters. Int J GeoMech 2016;16(3):04015086.
[35] Jackson R. The dynamics of fluidized particles. Cambridge, U.K.; New York: Cambridge University Press; 2000.
[36] El Shamy U. *A Coupled Continuum-Discrete Fluid-Particle Model for Granular Soil Liquefaction*. PhD Thesis. Troy, NY: Rensselaer Polytechnic Institute; 2004.
[37] Chen W, Qiu T. Numerical simulations for large deformation of granular materials using smoothed particle hydrodynamics method. Int J GeoMech 2010. https://doi.org/10.1061/(asce)gm.1943-5622.0000149.
[38] Sun X, Sakai M, Yamada Y. Three-dimensional simulation of a solid–liquid flow by the DEM–SPH method. J Comput Phys 2013;248:147–76.
[39] Robinson M, Ramaioli M, Luding S. Fluid–particle flow simulations using two-way-coupled mesoscale SPH–DEM and validation. Int J Multiphas Flow 2014;59:121–34.
[40] Markauskas D, Kruggel-Emden H, Scherer V. Numerical analysis of wet plastic particle separation using a coupled DEM-SPH method. Powder Technol 2018;325:218–27.
[41] Markauskas D, Kruggel-Emden H. Coupled DEM-SPH simulations of wet continuous screening. Adv Powder Technol 2019;30(12):2997–3009.
[42] Yi He, Bayly AE, Hassanpour A, Muller F, Wu K, Yang D. A GPU-based coupled SPH-DEM method for particle-fluid flow with free surfaces. Powder Technol 2018;338:548–62.
[43] Fernandez JW, Cleary PW, Sinnott MD, Morrison RD. Using SPH one-way coupled to dem to model wet industrial banana screens. Miner Eng 2011;24(8):741–53.
[44] Sinnott MD, Cleary PW, Morrison RD. Combined DEM and SPH simulation of overflow ball mill discharge and trommel flow. Miner Eng 2017;108:93–108.
[45] Cleary PW. Prediction of coupled particle and fluid flows using DEM and SPH. Miner Eng 2015;73:85–99.
[46] Karunasena HCP, Senadeera W, Gu YT, Brown RJ. A coupled SPH-DEM model for micro-scale structural deformations of plant cells during drying. Appl Math Model 2014;38(15–16):3781–801.
[47] Wu K, Yang D, Wright N. A coupled SPH-DEM model for fluid-structure interaction problems with free-surface flow and structural failure. Comput Struct 2016;177:141–61.
[48] Gingold RA, Monaghan JJ. Smoothed particle hydrodynamics: theory and application to non-spherical stars. Mon Not Roy Astron Soc 1977;181(3):375–89.
[49] Lucy LB. A numerical approach to the testing of the fission hypothesis. Astron J 1977;82:1013–24.
[50] Monaghan JJ. Smoothed particle hydrodynamics. Annu Rev Astron Astrophys 1992;30(1):543–74.
[51] Monaghan JJ. Simulating free surface flows with SPH. J Comput Phys 1994;110(2):399–406.
[52] Anderson TB, Jackson R. Fluid mechanical description of fluidized beds. equations of motion. Ind Eng Chem Fundam 1967;6(4):527–39.
[53] Dehnen W, Aly H. Improving convergence in smoothed particle hydrodynamics simulations without pairing instability. Mon Not Roy Astron Soc 2012;425(2):1068–82.
[54] Morris JP, Fox PJ, Zhu Y. Modeling low Reynolds number incompressible flows using SPH. J Comput Phys 1997;136(1):214–26.
[55] Monaghan JJ. SPH without a tensile instability. J Comput Phys 2000;159(2):290–311.
[56] Adami S, Hu XY, Adams NA. A generalized wall boundary condition for smoothed particle hydrodynamics. J Comput Phys 2012;231(21):7057–75.
[57] Bardet JP, Huang Q. Numerical modeling of micropolar effects in idealized granular materials. Mech. Granular Mater. Powder Syst. 1992;37:85–91.
[58] Bardet JP. Observations on the effects of particle rotations on the failure of idealized granular materials. Mech Mater 1994;18(2):159–82.
[59] Iwashita K, Oda M. Rolling resistance at contacts in simulation of shear band development by dem. J Eng Mech 1998;124(3):285–92.
[60] Oda M, Konishi J, Nemat-Nasser S. Experimental micromechanical evaluation of strength of granular materials: effects of particle rolling. Mech Mater 1982;1(4):269–83.
[61] Calvetti F, Combe G, Lanier J. Experimental micromechanical analysis of a 2d granular material: relation between structure evolution and loading path. *Mechanics of Cohesive-frictional Materials*. Int. J. Exper., Modell. Comput. Mater. Struct. 1997;2(2):121–63.
[62] Misra A, Jiang H. Measured kinematic fields in the biaxial shear of granular materials. Comput Geotech 1997;20(3–4):267–85.
[63] Itasca Consulting Group. PFC3D (Particle Flow Code in 3 Dimensions). 2019. Minneapolis, MN.
[64] Markauskas D, Kruggel-Emden H, Sivanesapillai R, Steeb H. Comparative study on mesh-based and mesh-less coupled CFD-DEM methods to model particle-laden flow. Powder Technol 2017;305:78–88.
[65] Ergun S. Fluid flow through packed columns. Chem Eng Prog 1952;48:89–94.
[66] Iai S, Tobita T, Nakahara T. Generalised scaling relations for dynamic centrifuge tests. Geotechnique 2005;55(5):355–62.
[67] El Shamy U, Aydin F. Multiscale modeling of flood-induced piping in river levees. J Geotech Geoenviron Eng 2008;134(9):1385–98.
[68] Carman PC. Fluid flow through granular beds. Trans Inst Chem Eng 1937;15:150–66.
[69] El Shamy U, Abdelhamid Y. Some aspects of the impact of multidirectional shaking on liquefaction of level and sloping granular deposits. J Eng Mech 2017;143(1):C4016003.
[70] Edwards SF. The equations of stress in a granular material. Physica A 1998;249:226–31.
[71] Onoue A. Diagrams considering well resistance for designing spacing ratio of gravel drains. Soils Found 1988;28(3):160–8.
[72] Brennan AJ, Madabhushi SPG. Effectiveness of vertical drains in mitigation of liquefaction. Soil Dynam Earthq Eng 2002;22(9):1059–65.